



OPEN Device grade solid-state pouch and coin cell supercapacitors dual assembly using consumed battery waste to best utilization

T. Kedara Shivasharma¹, Rajulal Sahu¹, Mayur Thosare¹, Debalaya Sarker², Uday Deshpande² & Babasaheb R. Sankapal¹✉

Recycling of the e-waste is a crucial concern to maintain healthy ecosystem as the technological advancement of electronic industries leads to the disposal of old electronic gadgets. The sustainable and green approaches to utilize these e-wastes in novel technologies is the prime requisite. Hence, present work aimed to use spent dry cell battery waste extracted Mn_2O_3 -C- ZnO_2 (MCZ) composite as e-waste to design and develop prototype device grade solid-state pouch and coin cells supercapacitors. Structural, surface morphological, compositional and oxidation state analysis of extracted materials have been performed. To optimise the electrochemical properties, the extracted waste battery material coated on stainless steel have been used in three electrode configuration followed by fabrication of symmetric solid-state device embedded with PVA- NaClO_4 gel electrolyte in dual assembly as prototype pouch (area 4 cm x 4.5 cm) and coin (diameter 16 mm) cells which delivered specific capacitance of 49.69 F g^{-1} at 5 mV s^{-1} and 7.93 F g^{-1} at 25 mV s^{-1} , respectively with remarkable potential window of 2 V along with energy density of 5.32 Wh kg^{-1} (@ power density 231.48 W kg^{-1}) and 0.44 Wh kg^{-1} (@ power density of 291.67 W kg^{-1}), respectively. Formed prototype device have been used to demonstrate practical applicability as TRL-3 through powering small fan, and 'VNIT' acronym LED panel. This work demonstrates the possibilities of converting waste battery material into liquid-free pouch and coin cell supercapacitor devices, resulting in sustainable and economic benefits.

Keywords Supercapacitors, Battery e-waste, Solid-state, Pouch cell, Coin-cell, TRL-3

Development of advanced portable, and compact technologies has created great demand for various kinds of batteries. More than 81% of hand-held batteries comprises of primary, non-rechargeable, and single use batteries, among which zinc-carbon batteries contributes 19%¹. Among total battery market, approximately 5–10% accounts for zinc carbon batteries, as they are cost effective and widespread availability. Even though production of zinc-carbon batteries is less in comparison to lithium-ion batteries, hundreds of millions of zinc-carbon batteries are produced every year². Nearly, three million tons of batteries were disposed globally every year, including zinc-carbon batteries, significant portion of which ends up in landfills³. The disposal of zinc-carbon batteries causes major environmental issues due to their toxic nature and the recycling rate is significantly low, around 30–40%². Zinc and manganese are the common components of zinc carbon batteries, the improper disposal of them can lead soil and water contamination. The small amount of zinc is very much essential, but it can be toxic in higher concentrations⁴. The manganese can cause health risks such as respiratory issues, and neurological effects⁵. These battery wastes were declared to be hazardous waste by Environmental Protection Agency (EPA), and their proper disposal is very much important for the protection of ecosystem and human health⁶.

The zinc-carbon battery consists of zinc anode, manganese oxide mixed with carbon powder as cathode, paste of ammonium and zinc chloride as electrolyte. The recycling of battery involves extraction of its constituents, cleaning from impurities and utilizing them in different applications. Physical, pyrometallurgical and hydrometallurgical processes were used for recycling of batteries⁷. The hydrometallurgical process includes acidic or basic leaching of electrode material and extraction of its constituents by physicochemical processes

¹Nano Materials and Device Laboratory, Department of Physics, Visvesvaraya National Institute of Technology, South Ambazari Road, Nagpur 440 010, M.S, India. ²UGC-DAE Consortium for Scientific Research, Indore, India. ✉email: brsankapal@gmail.com; brsankapal@phy.vnit.ac

such as precipitation, electrodeposition, and solvent extraction. Toxic hydrochloric, nitric, and sulfuric acids were used for leaching process⁸.

In last few years, electrochemical supercapacitors have become more innovative energy storage devices than batteries in quest of high-power density, fast charge discharge cycles, and extended life cycle. Hence, there is a drastic advancement in the supercapacitors with wide range applications in portable electronic industries, automobiles etc. Generally, supercapacitors store energy through either electric double layer capacitance (EDLC) or pseudocapacitance mechanisms. In EDLC mechanism, the electrolyte ions are absorbed electrostatically on electrode material which is mainly governed by large electrochemical active surface area. Nanostructured carbon materials such as carbon nanotubes, activated carbon, graphene oxide etc. comes under EDLC supercapacitor category^{9,10}. The pseudocapacitance arises from reversible redox activities, and intercalation mechanisms. Metal oxide¹¹, chalcogenides¹² phosphates, ferrites⁹ etc. nanomaterials were used as pseudocapacitive electrode material. The EDLC electrode materials possess high power density, extended life, and fast charge discharge, but they are limited from low energy density and specific capacitance. Contrarily, pseudocapacitors delivers good energy density but they failed to attain good power density, and long life. Recently attempts were made to form composites of EDLC and pseudocapacitive material in order to attain good energy density, power density along with cyclic stability.

In this regard, transition metal oxides like ruthenium oxide¹³, copper oxide¹⁴, manganese oxide¹⁵, cobalt oxide¹⁶, nickel oxide¹⁷, etc. were widely used electrode material for supercapacitor application. Manganese oxide owing to its multiple oxide states, high theoretical specific capacitance, redox behaviour, physical stability, large surface area finds its application in various fields such as energy storage¹⁵, catalysis¹⁸, water treatment¹⁹, anti-microbial activities²⁰ etc. Different methodologies have been developed like hydrothermal, chemical precipitation, sol-gel, green synthesis etc. to synthesize manganese oxide. But synthesis techniques might be complex and require toxic acids, but to achieve nano size particles, chemical methods are advantageous as it involves bottom-up approach²¹.

Present work is aimed at utilizing the spent zinc-carbon battery waste manganese oxide- carbon-zinc oxide (Mn_2O_3 -C- ZnO_2) by extracting simple method as pseudocapacitive-EDLC hybrid material. The extracted composite was coated on conducting stainless steel (SS) substrate and characterized through XRD, XPS, FE-SEM, and HR-TEM. Electrochemical analysis was carried out by studying cyclic voltammetry, galvanostatic charge discharge, and electrochemical impedance spectroscopy from electrode to solid-state device grade configured supercapacitor in the form of dual assembly as pouch and coin cells.

Results and discussion

Structural and composition analysis

Structural analysis of e-waste material obtained from spent battery was explored by X-ray diffraction analysis as shown in Fig. 1 (a). The composite of Mn_2O_3 , ZnO_2 , and C²² were detected, which were matched with Bragg's diffraction peaks of JCPDS cards (Mn_2O_3 : 73-1826, and ZnO_2 : 75-1526). The Mn_2O_3 peaks were observed at 2θ value of 18.87, 21.73, 28.71, 37.4, 41.94, 55.31, 56.69, 59.43, and 65.23° corresponding to hkl crystal planes of (0 0 2), (0 2 1), (2 1 2), (0 0 4), (1 3 3), (4 0 4), (3 4 3), (0 6 1), and (2 2 6), respectively. The carbon peak present at 26.71° corresponding to hkl plane of (0 0 2)²². The (1 0 1) hkl plane of ZnO_2 was present at 2θ value of 36.66°. Hence, Mn_2O_3 -C- ZnO_2 (MCZ) composite was concluded as a final product. The FTIR spectrum of battery derived material was represented in Fig. 1 (b). The absorption band observed at 593.23 cm^{-1} was correspond to the characteristic stretching of O-Mn-O²³. The band observed at 1099.02 cm^{-1} shows the C-O stretching bond and at 1591.9 cm^{-1} shows the C=C stretching vibration bond²⁴. The range 550 to 610 cm^{-1} was assigned to Mn-O-Mn stretching [35], 1000 to 1100 cm^{-1} was assigned to C-O stretching²⁵, and 1550 to 1650 cm^{-1} was assigned to C=C stretching²⁶. The absorption peak around 694.2 cm^{-1} is due to Zn-O vibrations present in the extracted material²⁷ showing the presence of Mn_2O_3 -C- ZnO_2 in the sample.

The chemical composition of spent battery extracted powder was further investigated through XPS analysis as presented in Fig. 2. The Fig. 2 (a) depicts the survey scan of powder extracted from spent battery, which shows

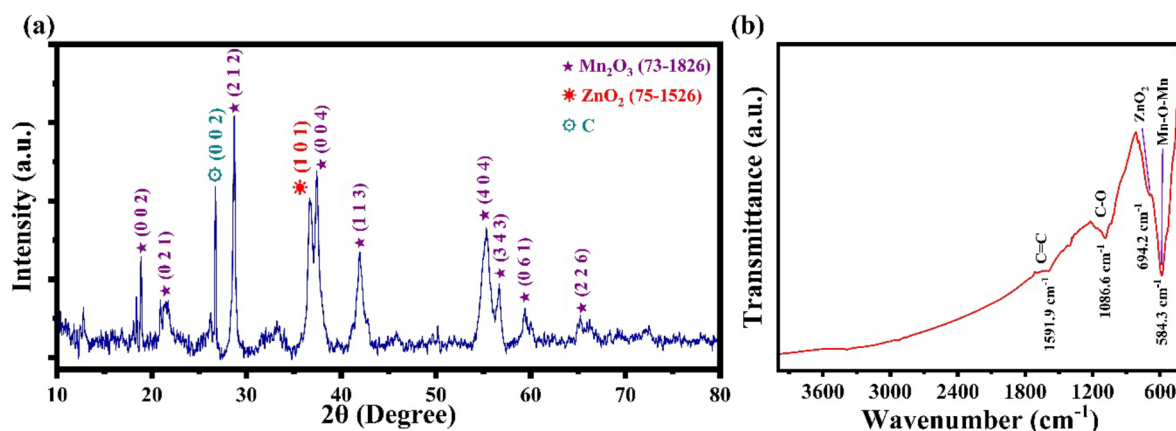


Fig. 1. (a) X-ray diffraction pattern, and (b) FTIR spectrum of powder extracted from spent battery waste.

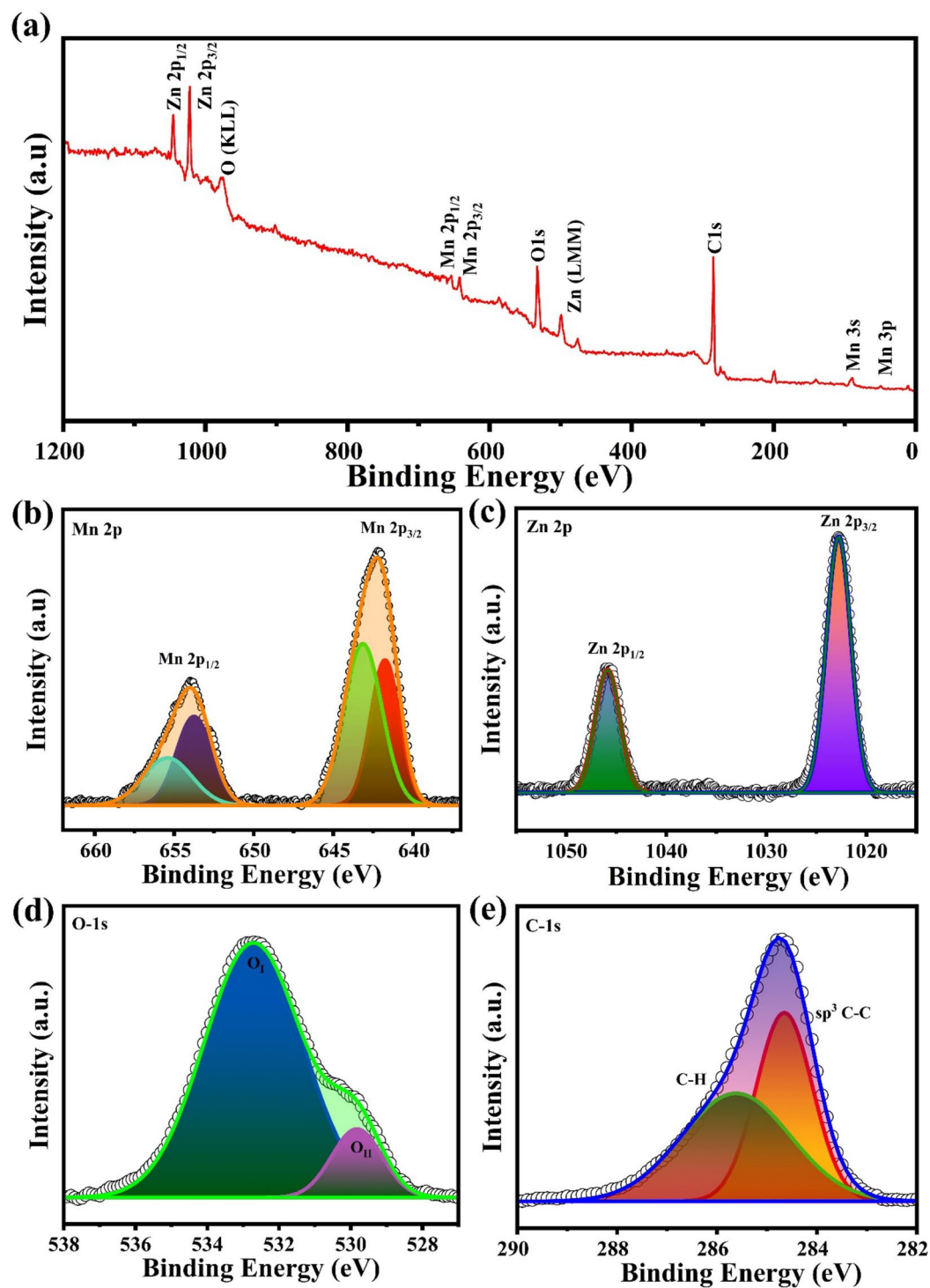


Fig. 2. (a) XPS wide scan survey of powder extracted from spent battery waste, narrow scan survey of (b) Mn 2p, (c) Zn 2p, (d) O 1s, and (e) C 1s.

the presence of Mn, C, O, and Zn. The detailed scan survey of Mn was shown in Fig. 2 (b). The deconvoluted peaks at 641.75, and 653.75 eV corresponds to the + 3 state of Mn $2p_{3/2}$, and Mn $2p_{1/2}$ respectively, whereas peaks at 643.14, and 655.43 eV corresponds to the + 4 state of Mn $2p_{3/2}$, and Mn $2p_{1/2}$ respectively^{28,29}. The multiple oxidation states on Mn might enhance the pseudocapacitive charge storage mechanisms. Figure 2 (c) shows the Zn spectra, with peak values of 1022.8, and 1046.0 eV correlated to Zn $2p_{3/2}$, and Zn $2p_{1/2}$, respectively³⁰. The oxygen high resolution XPS spectra was represented in Fig. 2 (d), which shows peaks at 529.8 (O_{II}) and 532.7 (O_I) eV corresponding to Mn and Zn oxygen bonds^{29,31}. The Fig. 2 (e) depicts the high resolution XPS spectra of carbon. The peaks at 284.65, and 285.62 eV corresponds to sp^3 C-C and C-H bonds, respectively³².

Morphological analysis

Surface morphology of powder was explored through FE-SEM analysis. The Fig. 3 (a, and b) confirmed the non-uniform agglomerated particles without any certain shape or orientation. The presence of manganese oxide, zinc oxide and carbon cannot be distinguished but they co-exist. Further morphological studies were carried out through HR-TEM analysis for the fine particles of powder and is shown in Fig. 3 (c). The high-resolution images of powder present the non-uniform agglomerated particles (Fig. 3 (d)). The SAED pattern is represented the Fig. 3 (e) which shows small spots making up concentric rings due to the Bragg reflection from crystallite indicating the polycrystallinity of the material. The SAED pattern shows the presence of (1 3 3), (4 0 4), and (2 2 6) crystal planes of Mn_2O_3 corresponding to d-spacing values of 2.15, 1.66, and 1.40 Å, respectively whereas the d-spacing 3.35 Å corresponds to the carbon (2 0 2) plane. The crystal planes (1 0 1) with d-spacing of 2.47 Å corresponds to ZnO_2 . These results of HR-TEM are well supported to the results obtained from XRD analysis.

Electrochemical analysis of Mn_2O_3 -C- ZnO_2 electrode

The reusability of the Mn_2O_3 -C- ZnO_2 composite (MCZ) derived from waste battery cell in supercapacitor applications was explored through different electrochemical characterization such as cyclic voltammetry (CV), galvanostatic charge discharge (GCD), and electrochemical impedance spectroscopy (EIS). The electrode preparation from MCZ composite is provided in supplementary information S2. The mass loading of the MCZ electrode was found to be 1.2 mg cm^{-2} . The initial electrochemical behaviour of material was scrutinized in three electrode configuration, and further potential applicability of electrodes were tested by fabricating prototype solid-state pouch and coin cell devices. Initial electrochemical investigation of MCZ electrodes were carried out using CV in 1 M concentrations of different (KOH, NaCl, NaClO_4 , LiClO_4 , LiCl, KCl) electrolytes to find out the most suitable where NaClO_4 exhibited superior performance (supplementary Fig. 1) and used further for the electrochemical analysis. Figure 4 (a) presents CV plots of MCZ electrodes in 1 M NaClO_4 electrolyte at different scan rate within the wide potential range of 0 to 1 V. EDLC based materials shows rectangular CV curves, while pseudocapacitive based material shows either redox peaks or non-rectangular CV curves. Even though metal oxides show prominent intercalation-deintercalation mechanisms in comparison with redox activities, they exhibit broad or no redox peaks in CV³⁷. The CV plots of MCZ electrode exhibit quasi rectangular shape indicating hybrid nature of electric double layer capacitive and intercalation assisted pseudocapacitive charge storage mechanism³⁸. The electric double layer charge storage originates from physical adsorption of electrolyte ions onto the electrode material while pseudocapacitive charge storage was due to intercalation of Na^+ ions into the Mn_2O_3 -C- ZnO_2 composite present in the electrode material. The CV plot retains the shape; exhibiting symmetric anodic and cathodic curve even at lower scan rate indicating electrochemical reversibility³⁹. The

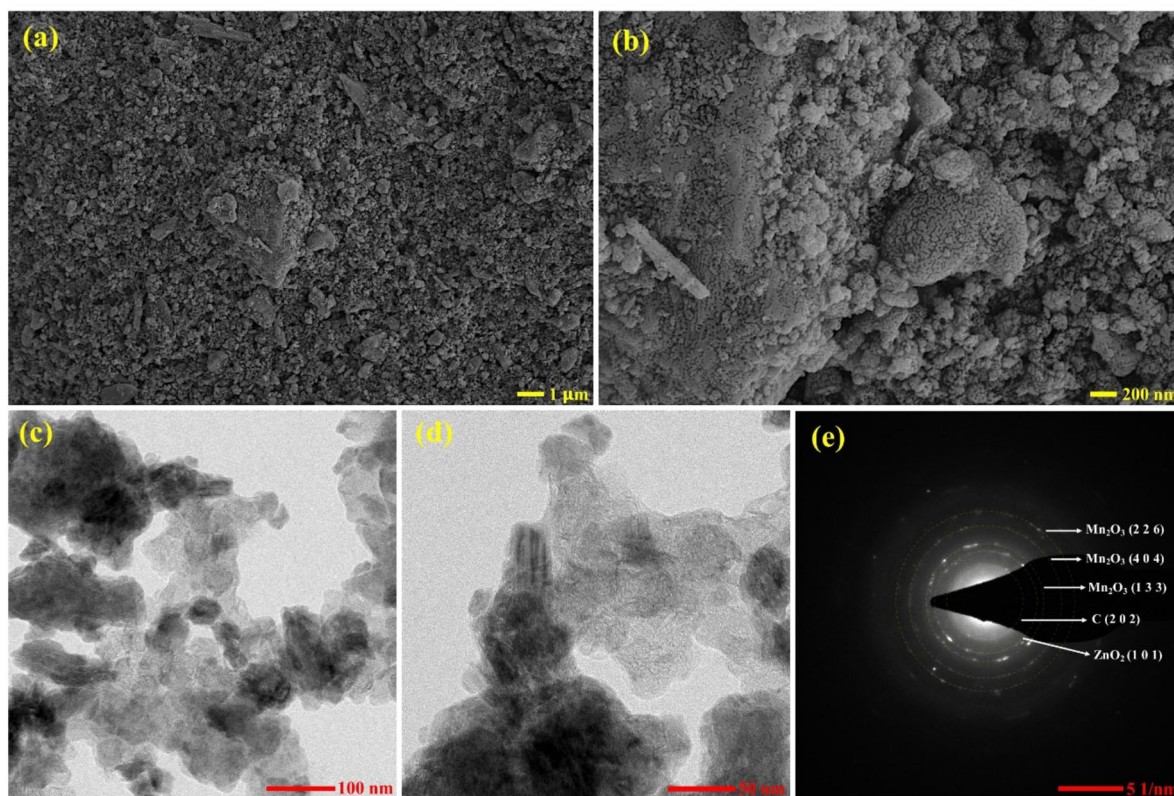


Fig. 3. (a-b) FE-SEM micrographs, (c-d) HR-TEM images, and (e) SAED pattern of powder extracted from spent battery waste.

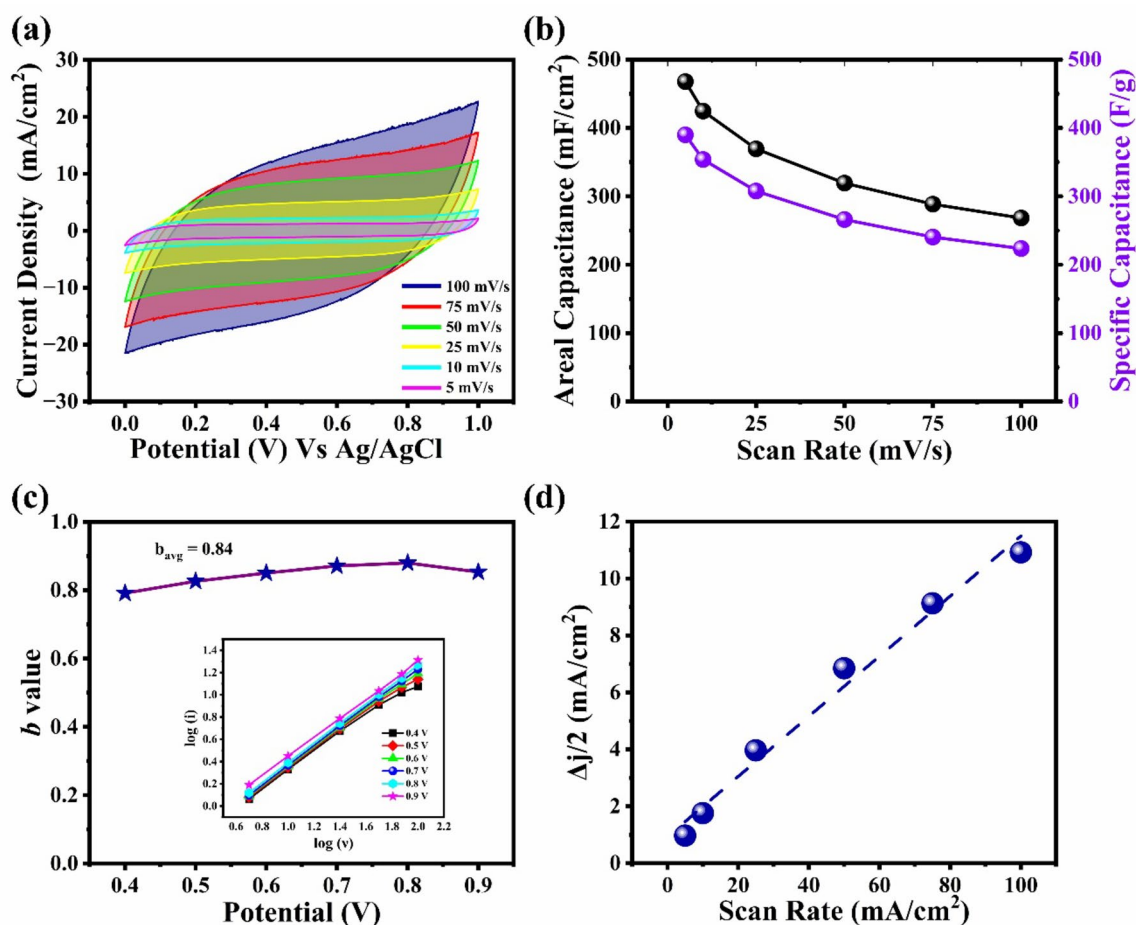


Fig. 4. (a) Cyclic voltammetry in the scan rate ranging from 5 to 100 mV s⁻¹, (b) specific capacitance with respect of different scan rates of electrode, (c) 'b' at different potential (inset: log(*i*) vs. log(*v*) plot) and (d) Δ*j*/2 vs. scan rate.

electrode exhibited specific capacitance of 223.63 F g⁻¹ (areal: 268.35 mF cm⁻²) at 100 mV s⁻¹ scan rate attaining maximum value of 389.86 F g⁻¹ (areal: 467.83 mF cm⁻²) at 5 mV s⁻¹ as electrolyte ions interact with electrode material to optimum level as it gets sufficient time at lower scan rate (Fig. 4 (b)). The nature of electrochemical charge storage was critically scrutinized through power law given by Eq. (1). In CV curves current at particular potential for different voltages were determined, and log(*i*) vs. log(*v*) was plotted which follows the Eq. (2).

$$i = av^b \quad (1)$$

$$\log(i) = \log(a) + b \log(v) \quad (2)$$

where *i* is the current density, *v* is the scan rate, 'a' and 'b' are the empirical constants. The value of 'b' shows the nature of charge storage. When, the 'b' value attains the value of unity, it depicts the surface capacitive charge storage mechanism. It shows pure diffusion-controlled mechanism when its value reaches 0.5⁴⁰. The 'b' value was determined from the slope of log(*i*) vs. log(*v*) graph plotted at different voltage ranges from 0.4 to 0.9 V (inset Fig. 4 (c)). Figure 4 (c) presents the 'b' value obtained at different potentials, and average value of 'b' was 0.84 indicating pseudocapacitive mechanism along with surface capacitive charge storage mechanisms.

The electrochemical active surface (ECSA) of electrode material taking part in electrochemical activities was calculated by using the Eq. (3). Mc Crory method of calculation of ECSA involves determination of surface involved in non-faradic electric double layer charge storage mechanism. Here, the non-faradic region with no evident faradic mechanisms in the CV curve needs to be identified. Earlier through power law we have calculated the 'b' value at different potentials. For ECSA calculation, CV was measured in the potential range of 0.5 to 0.9 V as "b" value (0.87) is much nearer to unity at potential 0.7 V (supplementary Fig. 2). The double layer capacitance (*C*_{DL} = 0.105 mF cm⁻²) was determined from the slope of plot of Δ*j*/2 vs. *v* (Fig. 4 (d)).

$$ECSA = \frac{C_{DL}}{C_s} \quad (3)$$

$$\frac{\Delta j}{2} = vC_{DL} \quad (4)$$

The C_s is the standard specific capacitance of electrode (area 1 cm²) with smooth surface, which significantly depends on the electrolyte, potential window, electrolyte concentration, and crystal structure. The universal accepted standard value of C_s for metal oxides is 40 μF cm⁻² ⁴¹. The ESCA of MCZ electrode was calculated to be 2625 cm² g⁻¹. The significantly high value of ECSA results in better charge storage capability of MCZ electrode. The hybrid nature of charge storage was quantitatively analyzed through calculating the charge stored by surface capacitive and diffusion-controlled mechanisms. The total charge storage (Q_t) originates from scan rate independent surface capacitive mechanism (Q_s) and inverse square root of scan rate dependent diffusion-controlled mechanism ($Q_d \propto v^{-0.5}$) ⁴².

$$Q_t = Q_s + Q_d \quad (5)$$

$$Q_t = Q_s + kv^{-0.5} \quad (6)$$

$$Q_t = \frac{\int_{i_1}^{f_1} i(V) dV}{m \cdot v} \quad (7)$$

The total charge stored was calculated through determining area under CV curves ($\int_{i_1}^{f_1} i(V) dV$) and using the Eq. (7). Figure 5 (a) depicts the Q_t vs. $v^{-0.5}$, intercept of which shows the charge stored through surface capacitive mechanisms. The electrode stored 49.70% charges through surface capacitive mechanism at 5 mV s⁻¹, which increases to 86.64% at 100 mV s⁻¹ indicating hybrid charge storage mechanism (Fig. 5 (b)).

Further, the electrochemical analysis was carried out through galvanostatic charge-discharge (GCD) at different current densities ranging from 2 to 4.5 mA cm⁻² within the same potential window (1 V) and is shown in Fig. 5 (c). The GCD curves presents hybrid nature of charge storage mechanism. The initial small rapid voltage drop in discharge curve originates from the internal resistance of the electrode material, which is followed by linear curve due to electric double layer charge storage mechanism. A curved part can be observed at near end of discharge curve indicating pseudocapacitive intercalation mechanism ⁴³. The electrode achieved highest specific capacitance of 197.34 F g⁻¹ (areal: 236.80 mF cm⁻²) at 2 mA cm⁻² current density, retaining 131.93 F g⁻¹ (areal: 158.31 mF cm⁻²) even at high current density 4.5 mA cm⁻² (Fig. 5 (d)). The Coulombic efficiency is the ratio of time needed to discharge and charge the electrode, which determines the electrochemical reversibility of electrode material. Figure 5 (e) depicts the coulombic efficiency at different current densities. The electrode achieved excellent coulombic efficiency of 100.93% at 2 mA/cm² which retained 98.49% at current density of 4.5 mA/cm². The GCD pots were helpful in calculating equivalent series resistance (ESR) of electrochemical system by measuring iR_{drop} of discharge curve. Figure 5 (f) represents the plot of iR_{drop} vs. current density, slope of which gives the ESR value. The minimum ESR value of 34.9 Ω indicates the low internal and diffusion resistance resulting in high power density of supercapacitor with least energy lost.

The electrochemical impedance analysis of the MCZ electrodes was carried out in the frequency regime of 100 mHz to 100 kHz to scrutinize the capacitive nature, resistive behaviour, diffusion and charge storage mechanisms. The Nyquist spectra of MCZ electrodes were plotted in Fig. 6 (a) and fitted with an equivalent circuit is as shown in inset Fig. 6 (a). The solution resistance (R_s) arises from the resistances at electrolyte and electrode interface, which can be seen as real axis intercept at high frequency region. The small semicircle at high frequency region indicates charge transfer resistance (R_{CT}) which originates from the electrochemical activities at electrode surface. Low value of R_s (2.46 Ω·cm²) and R_{CT} (11.81 Ω·cm²) indicates the better electrochemical activities ⁴⁴. The ion or charge separation at electrode-electrolyte interface results in double layer capacitance which was present as constant phase element (CPE_{DL}) ⁴⁵. The leakage resistance (R_L) in parallel with capacitive element (C_{DL}) signifies the contribution of pseudocapacitance attributed to the surface redox activities at electrode-electrolyte interface ⁴⁶. The 'W' represents the Warburg element depicting diffusion of ions into the electrode material at intermediate frequency region and it mainly arises from frequency dependent diffusion process. Constant phase element (CPE_L) presents pseudocapacitance due to potential dependent faradic charge transfer mechanism ⁴⁵. The material possessing 'n' ($CPE-n$) value in the range of 0.5 to 1 were considered to be pseudocapacitive, with more surface capacitive dominating when 'n' value reaches 1 and diffusion-controlled dominating when n value attains 0.5. The CPE_{DL} (n_{DL}) and CPE_L (n_L) were 0.71 and 0.74, respectively showing hybrid nature of charge storage ⁴⁷.

The accessibility of electrolyte ions into the active electrode material was studied through estimating diffusion coefficient. It can be calculated through the real impedance at low frequency region in Nyquist plot by using the equation provided in supplementary information S3. Figure 6 (b) depicts the real impedance vs. inverse square root of angular frequency. The diffusion coefficient was determined to be 9.9×10^{-16} cm² s⁻¹, smaller value of which shows the active diffusion of Na⁺ ions into the MCZ electrode through short path ways. The cyclic stability of MCZ electrode was carried out through 10,000 GCD cycles (Fig. 6 (c)). The capacitive retention of electrode initially increases to more than 125% till 2500 GCD cycles; might be due to the open up the active sizes of agglomerated particles providing enhanced electrochemical active surface area. Further, the capacitive retention gradually decreases after 2500 GCD cycles, and reaches 90.96% after 10,000 GCD cycles as material degradation might have happened.

Electrochemical analysis of prototype solid-state pouch cell device

To study the practical applicability of spent battery waste material in supercapacitor electrodes, prototype symmetric solid-state pouch cell devices was fabricated using NaClO₄ electrolyte embedded in PVA gel polymer

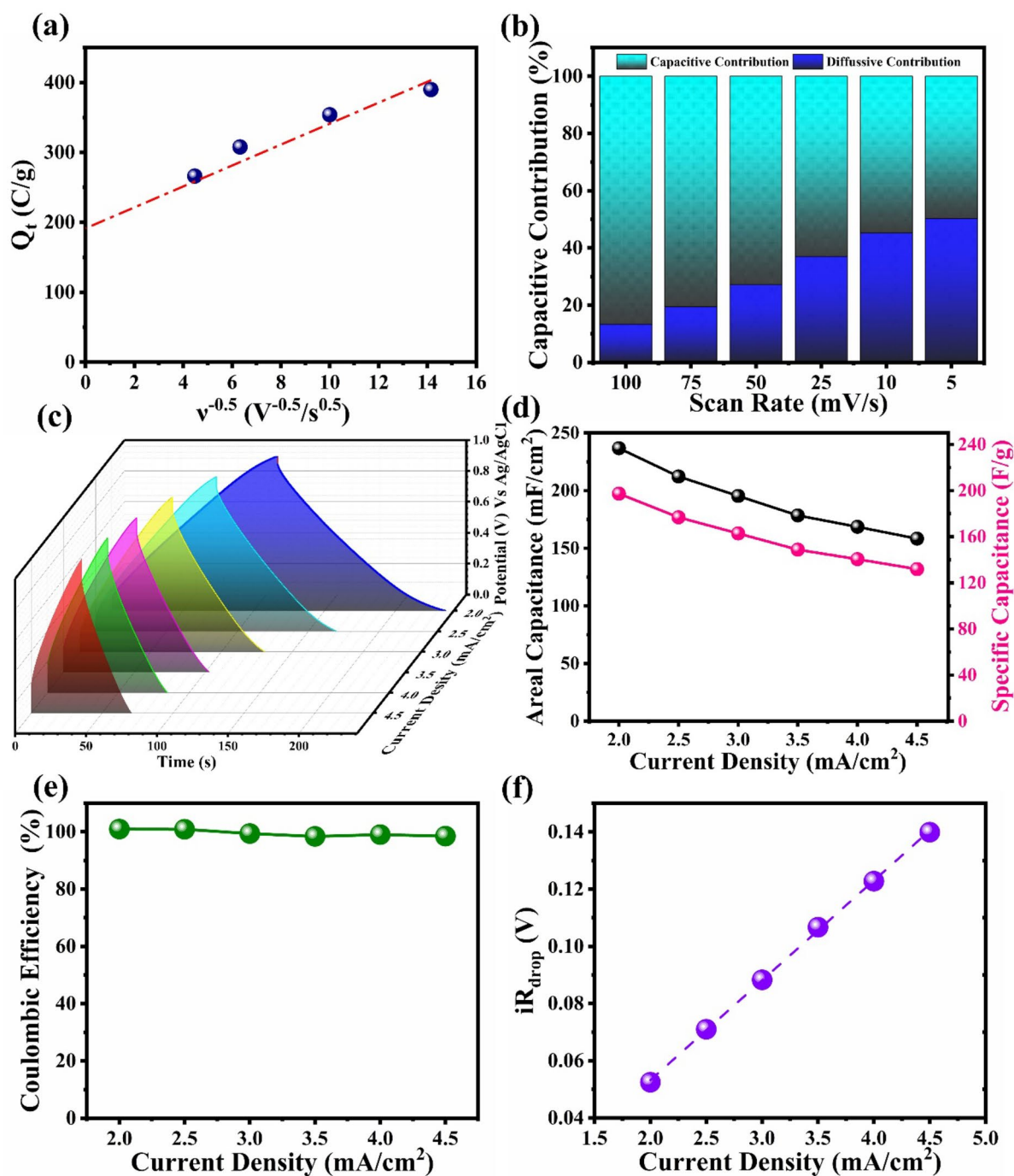


Fig. 5. (a) Q_t vs. $v^{-0.5}$ plot, (b) diffusion-controlled mechanism and surface capacitive mechanism contribution to total charge stored, (c) galvanostatic charge discharge plot at different current densities, (d) specific and areal capacitance at different current densities of electrode, (e) coulombic efficiency at different current density, and (f) iR_{drop} vs. current density.

(supplementary information S2). The optimization of solid-state pouch cell (schematic represented in Fig. 7 (a)) was performed in different potential window ranging from 1.4 to 2.0 V and shown in supplementary Fig. 4. The optimal potential window of 2 V was chosen and tested at varied scan rate from 100 to 5 mV s⁻¹ (inset Fig. 7 (b)). The non-rectangular nature of the CV plots with no significant redox peaks signifies the hybrid nature of the charge storage with pseudocapacitive intercalation mechanisms³⁸. The CV profile remains identical at varied scan rate indicating good electrochemical reversibility. The device showed specific capacitance of 5.77 F g⁻¹ (areal: 6.92 mF cm⁻²) at 100 mV s⁻¹, achieving maximum value of 49.69 F g⁻¹ (areal: 59.63 mF cm⁻²) at 5 mV s⁻¹ (Fig. 7 (b)). Figure 7 (c) shows the GCD plots at different currents. The GCD plot clearly depicts the non-triangular pseudocapacitive nature with initial voltage drop due to the internal resistance followed by

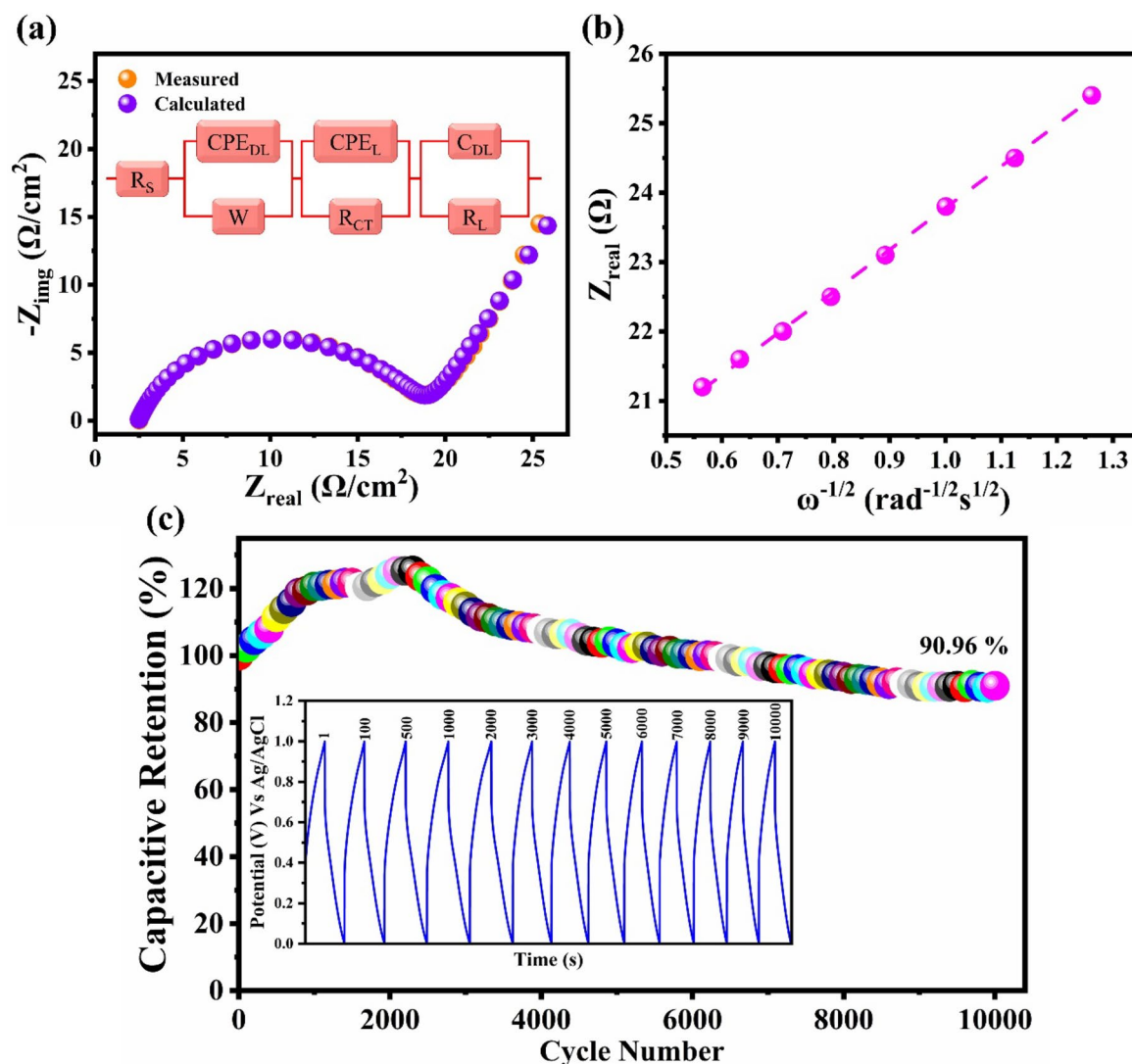


Fig. 6. (a) Nyquist plot of MCZ electrode (inset: equivalent circuit), (b) Z_{real} vs. $\omega^{-1/2}$, and (c) capacitive retention of electrode for 10,000 GCD cycles.

non-linear curve supported by diffusion-controlled mechanisms. Figure 7 (d) presents the specific capacitance of device at different currents, achieving highest value of 9.58 F g^{-1} (areal: 11.5 mF cm^{-2}) at 2.5 mA . The reduced electrochemical stability in comparison to electrode might be due to the hindrance to the electrode agglomerated electrode material to open up in PVA- NaClO_4 gel matrix. The EIS scrutiny was conducted to study the resistive behaviour, nature of charge storage and model the equivalent circuit same as that of electrode. Figure 7 (e) depicts the Nyquist plot of Z_{real} vs. $-Z_{\text{img}}$ in the frequency range of 100 mHz to 100 kHz . The obtained data was fitted with same equivalent circuit as that of electrode. The R_S resistance was determined to be 1.17Ω . Even though the R_S value of minimum the large R_{CT} value of 103.2Ω restrict the transfer of charge and/or ions between electrolyte gel polymer and electrode resulting in reduced specific capacitance⁴⁴. Analogues to electrode, the system contains CPE_{DL} due to ion or charge separation at electrode-electrolyte interface⁴⁵. The leakage resistance (R_L) in parallel with capacitive element (C_{DL}) originating from pseudocapacitance due to intercalation activities at electrode electrolyte interface. The Warburg element (W) indicating diffusion of ions through the polymer gel electrolyte into the electrode material at intermediate frequency region and CPE_L pseudocapacitance, resulting from potential dependent faradic charge transfer mechanism⁴⁵. Further, electrochemical stability analysis of pouch cell device was studied through 5000 GCD cycles. The capacitance gradually decreased and achieved capacitive retention of 83.02% (Fig. 8 (a)). As TRL-3, the practical application of prototype solid-state pouch cell was tested by powering small fan (Fig. 8 (b)), and 'VNIT' acronym LED penal (Fig. 8 (c)). The pouch cell was discharged for 12 s through small fan which was charged for 20 s , whereas discharged for 75 s through VNIT LED panel, which was charged for 10 s . The output voltage of the device was measured through voltmeter meter which showed values of 2.0 V (supplementary Fig. 5).

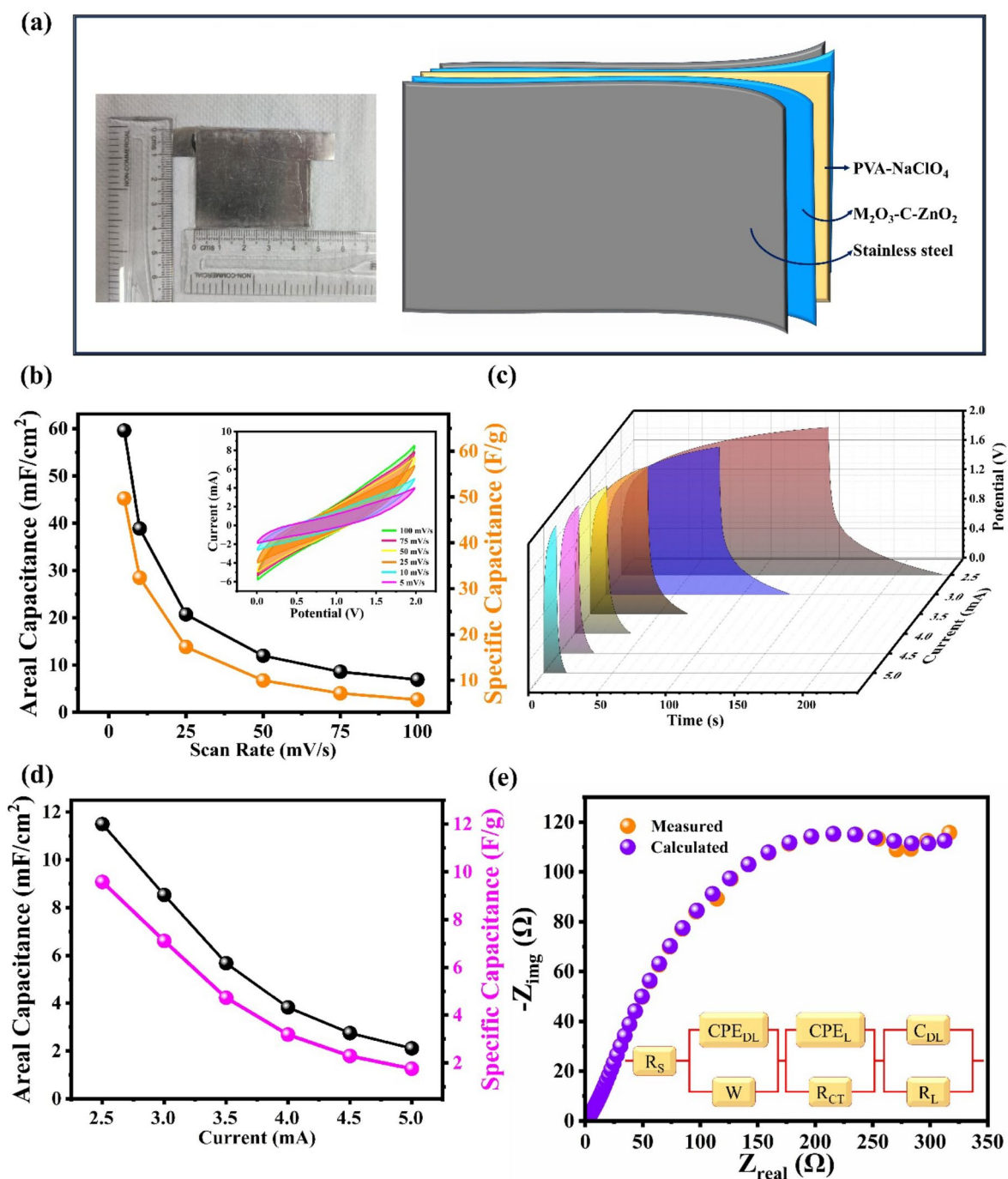


Fig. 7. (a) Schematic of solid-state pouch cell, (b) specific and areal capacitance of solid-state pouch cell at different scan rates (inset: cyclic voltammetry in the scan rate ranging from 5 to 100 mV s⁻¹), (c) galvanostatic charge discharge plot at different current densities, (d) specific and areal capacitance at different current of solid-state pouch cell, and (e) Nyquist plot of solid-state pouch cell (inset: equivalent circuit),

Electrochemical analysis of prototype solid-state coin cell device

Coin-cell type supercapacitors are emerging as important gadget in new advanced electronics for many portable electronic devices. If it is in solid-state configuration, it has many advantages including non-leakage tendency leading to complete damage of electronic devices. In this regard, designed symmetric coin cell schematic is presented in inset of Fig. 9 (a) which was fabricated by using PVA-NaClO₄ as polymer gel electrolyte (supplementary information S2). Figure 9 (a) shows the cyclic voltammetry in the potential window of 2 V of MCZ coin cell at different scan rates. The CV profiles were quite similar to that of pouch cell with non-rectangular nature with no significant redox peaks indicating intercalation mechanism with surface capacitive charge storage nature³⁸. It achieved maximum specific capacitance of 7.93 F g⁻¹ (areal: 9.51 mF cm⁻²) at 25 mV

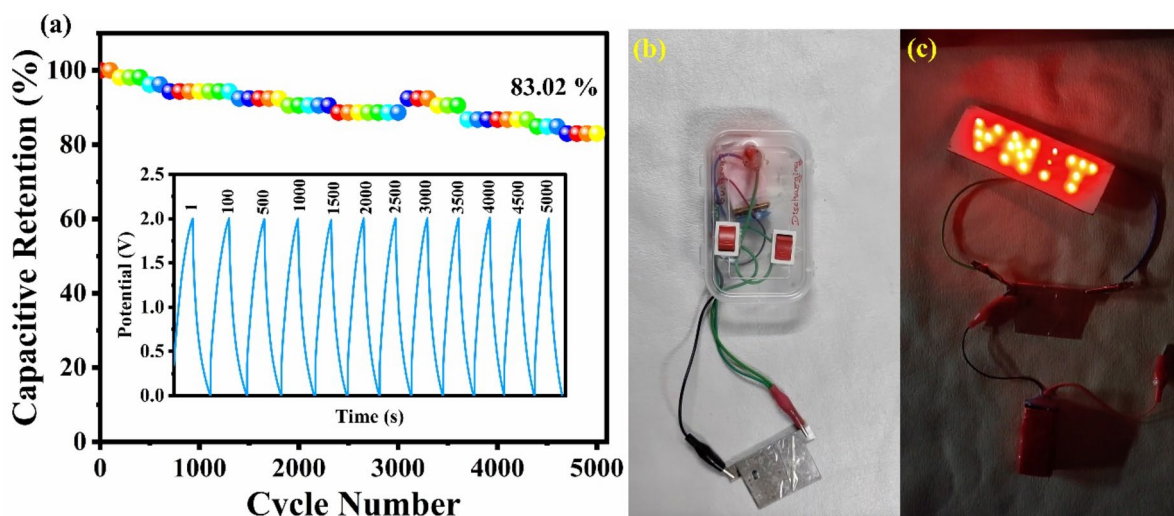


Fig. 8. (a) capacitive retention of MCZ solid-state pouch cell for 5000 GCD cycles, practical application of solid-state pouch cell through powering (b) small fan, and (c) VNIT LED panel.

s^{-1} , retaining 2.32 F g^{-1} (areal: 2.78 mF cm^{-2}) even at 100 mV s^{-1} demonstrated in supplementary Fig. 6. The GCD plot of MCZ coin cell was illustrated in Fig. 9 (b); presenting the pseudocapacitive type of charge storage with initial potential drop arising from the internal resistive nature of coin cell, followed by non-linear curve⁴³ and attained maximum specific capacitance of 0.78 F g^{-1} (areal: 0.95 mF cm^{-2}) at 0.7 mA current (Fig. 9 (c)). Figure 9 (d) depicts the Nyquist plot of coin cell in the frequency range of 100 mHz to 100 kHz and the obtained data was fitted with same equivalent circuit as that of electrode and solid-state pouch cell. The R_s and R_{CT} value are found to be 1.66 and $22.72, \Omega$ respectively. Even though silver paste was applied in-between the contacts to reduce the contact resistance, the coin cell suffered from high leakage current, as it showed minimum leakage resistance R_L of 0.57Ω resulting in low specific capacitance⁴⁴. The circuit also consist of C_{DL} , CPE_{DL} , CPE_L and Warburg element as that of pouch cell device. The cyclic stability analysis of solid-state coin cell was conducted by running GCD for 5000 cycles, which achieved capacitive retention of 57.14% (figure 9 (e)). The capacitance value of solid-state coin cell was reduced gradually till 4000 cycles and attained stable value of 57.14% at 4000 cycles. The Ragone plot of pouch and coin cell devices are presented in Fig. 9 (f) where the pouch cell achieved maximum energy density of 5.32 Wh kg^{-1} at the expense of power density 231.48 W kg^{-1} and the coin cell device achieved maximum energy density of 0.44 Wh kg^{-1} at the power density of 291.67 W kg^{-1} .

Conclusion

Utilization of battery waste $\text{Mn}_2\text{O}_3\text{-C-ZnO}_2$ composite has been successfully demonstrated towards device grade development of prototype solid-state pouch and coin cell assemblies by initially optimizing through single electrode configuration in liquid electrolyte. The waste powder derived from the dry cell was processed through chemical methods to obtain $\text{Mn}_2\text{O}_3\text{-C-ZnO}_2$ composite. The polycrystalline manganese oxide-carbon composite with presence of zinc oxide exhibited non-uniform morphology in FE-SEM and HR-TEM analysis. The FTIR and XPS analysis confirmed the presence of manganese oxide and carbon in the waste material from battery waste along with inclusion of Zn-O component. The extracted $\text{Mn}_2\text{O}_3\text{-C-ZnO}_2$ composite electrode exhibited specific capacitance of 389.86 F g^{-1} (areal: $267.83 \text{ mF cm}^{-2}$) at 5 mV s^{-1} scan rate and 197.34 F g^{-1} (areal: $236.80 \text{ mF cm}^{-2}$) at 2 mA cm^{-2} current density with potential window of 1 V in 1 M NaClO_4 with 90.96% capacitive retention after 10,000 GCD cycles. The electrode was further used to fabricate solid-state device and coin cell supercapacitor. The solid-state pouch and coin cell devices fabricated with Na^+ ions embedded in PVA gel polymer yields highest specific capacitance of 49.69 F g^{-1} (areal: 59.63 mF cm^{-2}) at 5 mV s^{-1} , and 7.93 F g^{-1} (areal: 9.51 mF cm^{-2}) at 25 mV s^{-1} , respectively with remarkable wide voltage window of 2 V . The maximum energy density of 5.32 Wh kg^{-1} and 0.44 Wh kg^{-1} at power density 231.48 W kg^{-1} and 291.67 W kg^{-1} have been achieved for pouch and coin cell devices, respectively. Practical applicability through powering small fan, and 'VNIT' acronym LED panel explores the potential for repurposing battery waste materials towards prototype device grade supercapacitive energy storage, offering both sustainable and economic advantages.

Methods

Materials

Discharged dry cell battery of Eveready Company, India, whereas 98% sulphuric acid (H_2SO_4) of Merck, PVDF (Polyvinylidene fluoride) of Sigma Aldrich, and NMP (N-Methylpyrrolidone) of Loba Chemie company were used.

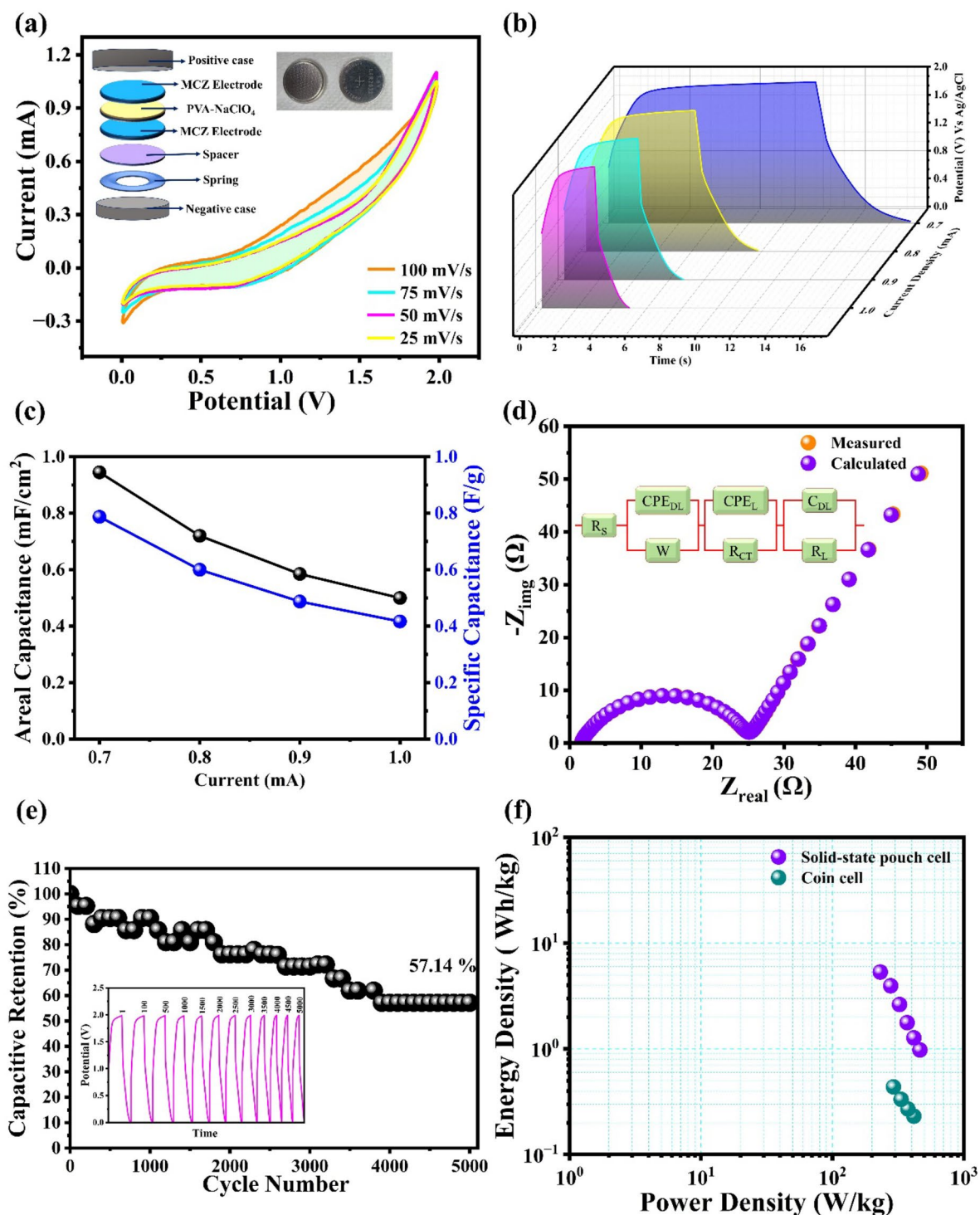


Fig. 9. (a) Cyclic voltammetry in the scan rate ranging from 5 to 100 mV s^{-1} (inset: schematic of solid-state coin cell), (b) galvanostatic charge discharge plot at different current densities, (c) specific and areal capacitance of coin cell at different currents, (d) Nyquist plot of solid-state coin cell, (e) cyclic stability of solid-state coin cell, and (f) ragone plot of solid-state pouch and coin cell.

Extraction of manganese oxide- carbon- zinc oxide composite

The Everyday dry cell battery was first dismantled and then cathode powder manganese oxide-carbon-zinc dioxide ($\text{Mn}_2\text{O}_3\text{-C-ZnO}_2$), hereafter termed as MCZ was taken out. The extracted powder was finely grinded. 5 gm of extracted powder was mixed with 90 ml of double distilled water to that 10 ml of H_2SO_4 was added, kept it for stirring for 30 min and rinsed 8–10 times to remove some metal impurities, followed by filtering and drying of the powder over night at 80 °C and fine grinding.

Data availability

The datasets used and/or analysed during the current study available from the corresponding author on reasonable request.

Received: 22 October 2024; Accepted: 28 March 2025

Published online: 04 August 2025

References

- Farzana, R., Hassan, K. & Sahajwalla, V. Manganese oxide synthesized from spent Zn-C battery for supercapacitor electrode application. *Sci. Rep.* **9**, 1–12 (2019).
- Battery Council International Home | Battery Council International. <https://www.batterycouncil.org/>
- IEA – International Energy Agency. <https://www.iea.org/>
- Khalef, R. N. et al. Heavy Metal's environmental impact. *Environ. Impact Remediation Heavy Met.* <https://doi.org/10.5772/INTECHOPEN.103907> (2022).
- Gandhi, D., Rudrashetti, A. P. & Rajasekaran, S. The impact of environmental and occupational exposures of manganese on pulmonary, hepatic, and renal functions. *J. Appl. Toxicol.* **42**, 103–129 (2022).
- Hazardous Waste | US EPA. <https://www.epa.gov/hw>
- Espinosa, D. C. R., Bernardes, A. M. & Tenório, J. A. An overview on the current processes for the recycling of batteries. *J. Power Sources*. **135**, 311–319 (2004).
- Bernardes, A. M., Espinosa, D. C. R. & Tenório, J. A. Recycling of batteries: a review of current processes and technologies. *J. Power Sources*. **130**, 291–298 (2004).
- Sankapal, B. R., Gajare, H. B., Karade, S. S. & Dubal, D. P. Anchoring Cobalt oxide nanoparticles on to the surface multiwalled carbon nanotubes for improved supercapacitive performances. *RSC Adv.* **5**, 48426–48432 (2015).
- Sankapal, B. R., Setyawati, K., Chen, J. & Liu, H. Electrical properties of air-stable, iodine-doped carbon-nanotube-polymer composites. *Appl. Phys. Lett.* **91**, 173103 (2007).
- Raut, S. S., Bisen, O. & Sankapal, B. R. Synthesis of interconnected needle-like Bi₂O₃ using successive ionic layer adsorption and reaction towards supercapacitor application. *Ionics (Kiel)*. **23**, 1831–1837 (2017).
- Raut, S. S., Dhobale, J. A. & Sankapal, B. R. SILAR deposited Bi₂S₃ thin film towards electrochemical supercapacitor. *Phys. E Low Dimens Syst. Nanostruct.* **87**, 209–212 (2017).
- Kim, J. Y. et al. Template-Free synthesis of ruthenium oxide nanotubes for High-Performance electrochemical capacitors. *ACS Appl. Mater. Interfaces*. **7**, 16686–16693 (2015).
- Enaïet Allah, A., Mohamed, E., Ghanem, M. A. & Ahmed, A. M. Chemical synthesis and super capacitance performance of novel CuO@Cu 4 O 3 /rGO/PANI nanocomposite electrode. *RSC Adv.* **14**, 13628–13639 (2024).
- Liu, J. et al. MnO₂-based materials for supercapacitor electrodes: challenges, strategies and prospects. *RSC Adv.* **12**, 35556–35578 (2022).
- Afzal, A. M. et al. Enhancing the Performance of Cobalt-based Oxide Electrode Material for Asymmetric Supercapacitor Devices. *ChemistrySelect* **8**, e202300440 (2023).
- Shah, A., Senapati, S., Murthy, H. C. A., Singh, L. R. & Mahato, M. Supercapacitor performance of NiO, NiO-MWCNT, and NiO-Fe-MWCNT composites. *ACS Omega*. **8**, 33380–33391 (2023).
- Wang, J. et al. Manganese oxide-based catalysts for the sustainable synthesis of value-added chemicals through oxidation processes: a critical review and perspectives for the future. *Green Chem.* **26**, 2365–2383 (2024).
- Jia, L., Zhou, Q., Li, Y. & Wu, W. Application of manganese oxides in wastewater treatment: biogeochemical Mn cycling driven by bacteria. *Chemosphere* **336**, 139219 (2023).
- Saod, W. M., Hamid, L. L., Alaallah, N. J. & Ramizy, A. Biosynthesis and antibacterial activity of manganese oxide nanoparticles prepared by green tea extract. *Biotechnol. Rep.* **34**, e00729 (2022).
- Nair, P. K. et al. Semiconductor thin films by chemical bath deposition for solar energy related applications. *Solar Energy Materials and Solar Cells*. **52**(3–4), 313–344. [https://doi.org/10.1016/S0927-0248\(97\)00237-7](https://doi.org/10.1016/S0927-0248(97)00237-7) (1998). ISSN 0927-0248.
- Kalagatur, N. K. et al. Application of activated carbon derived from seed shells of *Jatropha Curcas* for decontamination of Zearalenone Mycotoxin. *Front. Pharmacol.* **8**, 308339 (2017).
- Pugazhavadivu, K. S., Ramachandran, K. & Tamilarasan, K. Synthesis and characterization of Cobalt doped manganese oxide nanoparticles by chemical route. *Phys. Procedia*. **49**, 205–216 (2013).
- Interpreting infra-red spectra. <https://www.chemguide.co.uk/analysis/ir/interpret.html>
- Zappiello, C. D. et al. Solid phase extraction to On-Line preconcentrate trace cadmium using chemically modified Nano-Carbon black with 3-Mercaptopropyltrimethoxysilane. *J. Braz Chem. Soc.* **27**, 1715–1726 (2016).
- Liu, Y. et al. Efficient Adsorption of Sulfamethazine onto Modified Activated Carbon: A Plausible Adsorption Mechanism. *Sci. Rep.* **7**, 1–12 (2017).
- Taghizadeh, S. M. et al. Green and economic fabrication of zinc oxide (ZnO) nanorods as a broadband UV blocker and antimicrobial agent. *Nanomaterials* **2020**, **10**, Page 530 (10), 530 (2020).
- Amano, M. E., Betancourt, I., Arellano-Jimenez, M. J., Sánchez-Llamazares, J. L. & Sánchez-Valdés, C. F. Magnetocaloric response of submicron (LaAg)MnO₃ manganite obtained by pechini method. *J. Solgel Sci. Technol.* **78**, 159–165 (2016).
- Wang, M. et al. Efficiently enhancing electrocatalytic activity of α-MnO₂ Nanorods/N-Doped Ketjenblack carbon for oxygen reduction reaction and oxygen evolution reaction using facile regulated hydrothermal treatment. *Catalysts* **2018**, **8**, 138 (2018).
- Xu, D., Fan, D. & Shen, W. Catalyst-free direct vapor-phase growth of Zn_{1-x}Cu_xO micro-cross structures and their optical properties. *Nanoscale Res. Lett.* **8**, 1–9 (2013).
- Sahai, A. & Goswami, N. Structural and optical investigations of oxygen defects in zinc oxide nanoparticles. *AIP Conf. Proc.* **1665**, 050023 (2015).
- Morais, A., Alves, J. P. C., Lima, F. A. S., Lira-Cantu, M. & Nogueira, A. F. Enhanced photovoltaic performance of inverted hybrid bulk-heterojunction solar cells using TiO₂/reduced graphene oxide films as electron transport layers. (2015). <https://doi.org/10.1117/1.JPE.5.057408> **5**, 057408.
- Rodríguez-Romero, J., Ruiz de Larramendi, I. & Goikolea, E. Nanostructured manganese dioxide for hybrid supercapacitor electrodes. *Batteries* **2022**, **8**, 263 (2022).
- Chou, J. C. et al. RuO₂/MnO₂ core-shell nanorods for supercapacitors. *J. Mater. Chem. Mater.* **1**, 8753–8758 (2013).
- Hwang, J. Y. et al. Direct Preparation and processing of graphene/RuO₂ nanocomposite electrodes for high-performance capacitive energy storage. *Nano Energy*. **18**, 57–70 (2015).
- Jayakumar, S., Santhosh, P. C., Mohideen, M. M. & Radhamani, A. V. A comprehensive review of metal oxides (RuO₂, Co₃O₄, MnO₂ and NiO) for supercapacitor applications and global market trends. *J. Alloys Compd.* **976**, 173170 (2024).
- Najib, S. et al. Tailoring morphology to control defect structures in ZnO electrodes for high-performance supercapacitor devices. *Nanoscale* **12**, 16162–16172 (2020).
- Joseph, A. & Thomas, T. Recent advances and prospects of metal oxynitrides for supercapacitor. *Prog. Solid State Chem.* **68**, 100381 (2022).

39. Pajkossy, T. Analysis of quasi-reversible Cyclic voltammograms: transformation to scan-rate independent form. *Electrochem. Commun.* **90**, 69–72 (2018).
40. Joshi, A., Sahu, V., Singh, G. & Sharma, R. K. Performance enhancement of a supercapacitor negative electrode based on loofah sponge derived oxygen rich carbon through encapsulation of MoO₃ nanoflowers. *Sustain. Energy Fuels*. **3**, 1248–1257 (2019).
41. Wei, C. et al. Approaches for measuring the surface areas of metal oxide electrocatalysts for determining their intrinsic electrocatalytic activity. *Chem. Soc. Rev.* **48**, 2518–2534 (2019).
42. Isacfranklin, M. et al. Superior supercapacitive performance of Cu₂MnSnS₄ asymmetric devices. *Nanoscale Adv.* **3**, 486–498 (2021).
43. Mohd Abdah, M. A. A., Azman, N. H. N., Kulandaivalu, S. & Sulaiman, Y. Asymmetric supercapacitor of functionalised electrospun carbon fibers/poly(3,4-ethylenedioxythiophene)/manganese oxide/activated carbon with superior electrochemical performance. *Sci. Rep.* **9**, 1–9 (2019).
44. Laschuk, N. O., Bradley Easton, E. & Zenkina, O. V. Reducing the resistance for the use of electrochemical impedance spectroscopy analysis in materials chemistry. (2021). <https://doi.org/10.1039/d1ra03785d>
45. Wang, W. et al. Hydrous Ruthenium Oxide Nanoparticles Anchored to Graphene and Carbon Nanotube Hybrid Foam for Supercapacitors. *Sci. Rep.* **4**, 1–9 (2014).
46. Fan, X., Ohlckers, P. & Chen, X. Tunable synthesis of Hollow Co₃O₄ nanoboxes and their application in supercapacitors. *Appl. Sci.* (10), 1208 (2020).
47. Allagui, A., Freeborn, T. J., Elwakil, A. S. & Maundy, B. J. Reevaluation of Performance of Electric Double-layer Capacitors from Constant-current Charge/Discharge and Cyclic Voltammetry. *Sci. Rep.* **6**, 1–8 (2016).

Acknowledgements

Authors gratefully acknowledge UGC-DAE-CSR (CRS/2022-23/01/653) and DST-FIST (SR/FST/PSI/2017/5 (C)) projects.

Author contributions

T.K.S.: Conceptualization, Methodology, Validation, Formal analysis, Investigation, Data Curation, Writing-original draft, Visualization. R.S.: Methodology, Formal analysis, Investigation, Data Curation, Writing- Review and Editing. M.T.: Formal analysis, Methodology, Investigation, Writing- Review and Editing. D.S.: Investigation, Formal analysis, Writing- Review and Editing. U.D.: Investigation, Formal analysis, Writing- Review and Editing. B.R.S.: Validation, Visualization, Resources, Writing- Review and Editing, Supervision, Project administration.

Declarations

Competing interests

The authors declare no competing interests.

Additional information

Supplementary Information The online version contains supplementary material available at <https://doi.org/10.1038/s41598-025-96426-4>.

Correspondence and requests for materials should be addressed to B.R.S.

Reprints and permissions information is available at www.nature.com/reprints.

Publisher's note Springer Nature remains neutral with regard to jurisdictional claims in published maps and institutional affiliations.

Open Access This article is licensed under a Creative Commons Attribution-NonCommercial-NoDerivatives 4.0 International License, which permits any non-commercial use, sharing, distribution and reproduction in any medium or format, as long as you give appropriate credit to the original author(s) and the source, provide a link to the Creative Commons licence, and indicate if you modified the licensed material. You do not have permission under this licence to share adapted material derived from this article or parts of it. The images or other third party material in this article are included in the article's Creative Commons licence, unless indicated otherwise in a credit line to the material. If material is not included in the article's Creative Commons licence and your intended use is not permitted by statutory regulation or exceeds the permitted use, you will need to obtain permission directly from the copyright holder. To view a copy of this licence, visit <http://creativecommons.org/licenses/by-nc-nd/4.0/>.

© The Author(s) 2025